ACS OMEGA

Open Access

http://pubs.acs.org/journal/acsodf

Article

Osteoinduction and Osteoconduction Evaluation of Biodegradable Magnesium Alloy Scaffolds in Repairing Large Segmental Defects in Long Bones of Rabbit Models

Shujun Liu, Ming Gao, Na Liu, Ruixin Li, Zhiyong Zhang, Yuan Yao, Weiming Wang, Lili Tan, and Nan Zhang*

Cite This: *ACS Omega* 2024, 9, 46419−46428

Read Online

ACCESS | Metrics & More | Article Recommendations

ABSTRACT: Magnesium (Mg) alloy scaffolds demonstrate promising potential for clinical applications in the repair of segmental bone defects. However, the specific mechanisms of osteoconduction and osteoinduction facilitated by these scaffolds themselves during the bone reconstruction process remain inadequately defined. This investigation systematically assesses the properties of MAO-coated Mg base implants both in vitro and in vivo. Furthermore, it elucidates the correlation between scaffold characteristics and bone regeneration in the repair of extensive long-bone defects, measuring up to 20 mm, without the use of additional bone graft materials. Electrochemical measurements and immersion tests conducted in vitro indicate that the MAO coating substantially enhances the corrosion resistance of the underlying Mg alloy. Meanwhile, the application of MAO coatings has been shown to significantly improve cytocompatibility, cellular adhesion, and osteogenic differentiation, as evidenced by the CCK-8 assays, ALP activity measurements, Western blot, and RT-qPCR in vitro. At 24 weeks postimplantation with the MAO-coated Mg alloy scaffold, the large segmental defects were effectively repaired concerning both integrity and continuity. The Micro-CT gradual replacement of old bone with new bone on the implant surface was observed by X-ray and Micro-CT. Meanwhile, the histological results indicated that the MAO-coated Mg alloy scaffold maintained a robust osteogenic response. In summary, the MAO-coated Mg alloy scaffold independently exhibits effective osteoconduction and osteoinduction, playing a significant role in bone repair function without the need for additional bone graft materials.

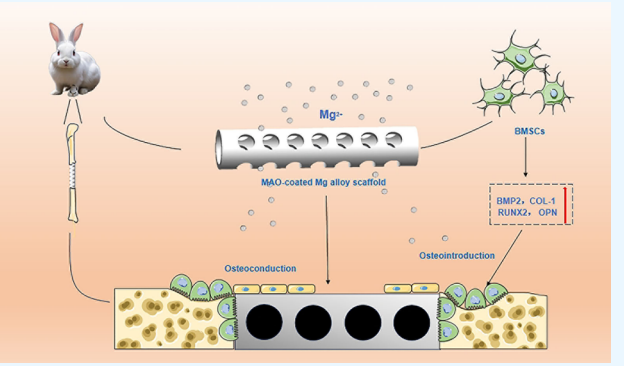

1. INTRODUCTION

A critical-size defect in long bones is characterized as a segmental bone defect that is more than twice (2.0−2.5 times) the diameter of the affected bone, typically resulting from severe damage due to infection, trauma, and tumor removal that surpasses the body's innate repair capabilities.[1,2] The primary surgical interventions in orthopedic surgery for addressing bone defects include autologous, allograft, and metal material transplantation.[3,4] However, challenges persist due to the limited supply of autologous bone grafts and associated donor site complications. Additionally, allograft surgery may cause immune rejection, culminating in graft failure.[5,6] Metals and alloys (such as titanium, tantalum, stainless steel, etc.) have been extensively utilized as orthopedic implants due to their significant role in bone defect[7] management despite concerns over ion release and stress shielding effect that may compromise surgical outcomes.[8,9] Moreover, permanent retention of some metal implants post reconstruction poses a long-term risk of infection in the body. Thus, the introduction of materials possessing superior bioactivity and biodegradability is critical to enhancing tissue regeneration and osseointegration during critical-size bone defect reconstruction.

Magnesium (Mg) and its alloys are deemed promising candidates for bone implant materials because of their high specific strength, elastic modulus comparable to bone, biodegradability, and good biocompatibility.[10,11] Additionally, the corrosion byproducts of Mg alloys, namely, magnesium hydroxide [$Mg(OH)_2$] and hydrogen (H_2), manifest as nontoxic entities that can be metabolically excreted through renal pathways.[12] Furthermore, increasing evidence supports

Received: August 18, 2024
Revised: October 14, 2024
Accepted: October 25, 2024
Published: November 8, 2024

Table 1. Composition of the Mg−Zn−Nd−Zr Alloy (Weight Percent)

	chemical composition							
Mg−Zn−Nd−Zr alloy	Mg	Zn	Nd	Zr	Si	Fe	Ni	Cu
wt %	balance	1.98	0.54	0.59	0.004	0.004	<0.005	<0.005

that Mg ions released from Mg alloy implants post surgery can promote bone regeneration and accelerate fracture healing.[13−15] In previous studies, we have also demonstrated that magnesium alloy not only exhibits commendable biocompatibility but also fosters osteogenic differentiation of BMSCs.[16,17] Upon its insertion into the organism, concomitant with the degradation of magnesium alloy implants, a pronounced enhancement in the rejuvenation and reconstitution of adjacent osseous tissue is notably observed.[18] Moreover, Mg-based implants are beneficial for the formation of new blood vessels[19] and exhibit antibacterial ability.[20] Mg-based orthopedic implants might offer a substantial advantage over non-Mg-based alternatives in treating bone ailments, as evidenced by related clinical trials conducted in Germany,[21] South Korea,[22] and China.[23] The aforementioned studies have unequivocally proven that magnesium alloys possess all of the requisite qualities to serve as the vanguard of a new era in orthopedic implant materials.

Despite numerous reports on the functionalization of Mg alloy materials for orthopedic implants, their application in repairing long-bone defects is limited due to the complex internal environments and stringent mechanical requirements. Smith et al.[24] first reported that the rolled AZ31 alloy was utilized to repair the critical-size defect in the ulna in rabbits, revealing that while the defect of the ulna was reconstructed within 12 weeks post implantation, the quality of new bone regeneration was compromised by the excess hydrogen produced during the rapid degradation of implants. In a previous study, we developed a novel Mg alloy scaffold by casting a hollow cylinder that mimics the shape of the cortical bone. This scaffold facilitates the inclusion of autologous bone within its core and features evenly distributed pores on its lateral walls to promote the growth of surrounding soft tissues and blood vessels.[25] Our findings indicated that the hydrogen production during degradation could be effectively managed by tailoring the corrosion behavior of Mg alloy, and the critical-size ulnar defect (15 mm) was successfully repaired within 12 weeks of implantation of the Mg alloy scaffold filled with autologous morselized bone,[26] suggesting Mg alloy as a viable implant material for the treatment of critical bone defects.

However, the process of repairing bone defects is intricate, requiring not only the implantation of bone grafts but also the intrinsic osteoinductive and osteoconductive properties of the implant material. Osteoinduction involves recruiting immature cells and stimulating their differentiation into preosteoblasts,[27] while osteoconduction facilitates bone growth directly on the implant's surface, a process described as "crawling substitution".[28] These mechanisms are crucial in the successful reconstruction of bone defects with implants. However, the specific role of osteoinduction and osteoconduction in the Mg alloy scaffold remains obscure in the reconstruction process, primarily because previous studies predominantly used autologous bone grafts. In the current study, we have developed an MAO-coated Mg alloy scaffold to assess its corrosion resistance both in vivo and in vitro. Additionally, to further explore the osteogenic properties of the scaffold itself in the process of repairing bone defects, we implanted empty MAO-coated Mg alloy scaffolds—without any bone graft materials—into extensive segmental defects (20 mm) in rabbits. After 24 weeks, we found that the MAO-coated Mg alloy scaffold successfully repaired the large segmental bone defect of the rabbit ulna, indicating that the scaffold itself had significant osteoconduction and osteoinduction.

2. MATERIALS AND METHODS

2.1. Preparation of the Mg Alloy Scaffold. A Mg−Zn−Nd−Zr alloy served as the substrate material, with its chemical composition detailed in Table 1. Cylindrical magnesium alloy tubes were fabricated by using a forging process, measuring 20 mm in length with an inner diameter of 3 mm and an outer diameter of 4 mm. These tubes featured 28 uniformly distributed pores, each with a diameter of 1.7 mm. A calcium−phosphorus self-sealing microarc oxidation (MAO) coating was applied to the scaffold surface using an electrolyte system comprising 1.2 g/L $Ca(OH)_2$, 8 g/L KF, and 64 g/L $NaPO_3$, under conditions of 360 V, 1000 Hz, a duty cycle of 40%, and a duration of 5 min. In addition, the samples were sectioned into disks (Φ10 mm × 3 mm) for corrosion testing and biological evaluation in vitro.

2.2. Corrosion Test. The corrosion resistance of coated samples was evaluated using an electrochemical workstation configured with a three-electrode system in Hank's solution at 37 ± 0.5 °C. Electrochemical impedance spectroscopy measurements were conducted across a frequency range of 10^{-2}−10^5 Hz at an amplitude of 10 mV. Potentiodynamic polarization was carried out at a scan rate of 0.5 mV/s. The corrosion potential (E_{corr}) and corrosion current density (I_{corr}) were determined by using the Tafel extrapolation method. The samples were immersed in Hank's solution for 28 days at 37 ± 0.5 °C with an exposure ratio of 30 mL/cm^2 as per ASTM.[29] Hank's solution was refreshed bidaily. Furthermore, the pH values and weight changes during the immersion period were recorded.

2.3. Toxicity Test. Assessment of the cytotoxicity of the samples was conducted via an indirect cell assay in accordance with ISO10993-5.[30] Rat bone marrow mesenchymal stem cells (BMSCs) were cultivated in minimum essential medium α (α-MEM, Gibco, USA) supplemented with 10% fetal bovine serum (FBS, Gibco, USA) under conditions of 37 °C, 5% CO_2, and 95% humidity. Subculturing occurred upon reaching 80−90% confluence. The sample was immersed in the complete culture medium at an extraction rate of 1.25 cm^2/mL for 1 day, and the resulting extract was used for subsequent in vitro cell experiments. The BMSCs were seeded in 96-well plates, allowing for cell attachment before the growth medium was replaced with the sample extract. Cells were incubated for further periods of 1, 3, and 5 days. Post incubation, 10 μL of Cell Counting Kit-8 (CCK-8, Beyotime, China) solution was added, and incubation was continued for 4 h. The absorbance of each well was measured at 450 nm by using a microplate reader.

For live/dead cell staining, after a gentle wash with PBS, 100 μL of live/dead staining reagent (Beyotime, China) was added. Cells were incubated for 30 min at 37 °C in the dark, after which the stain was removed, and the cells were washed again with PBS before 100 μL of normal medium. Live and dead cells were subsequently visualized by using a fluorescence microscope.

https://doi.org/10.1021/acsomega.4c07635
ACS Omega 2024, 9, 46419−46428

Table 2. Primer Sequences Used in RT-qPCR

gene	forward primer sequence (5′−3′)	reverse primer sequence (3′−5′)
BMP2	CCACCATGAAGAATCTTTGGA	GTGATAAACTCCTCCGTGG
Runx2	GCGCATTCCTCATCCCAGTA	GGTGGGGAGGATTGTGTCTG
COL-1	GTACATCAGCCCAAACCCCA	CAGGATCGGAACCTTCGCTT
OCN	CAGACAAGTCCCACACAGCA	CCAGCAGAGTGAGCAGAGAG
GAPDH	GGCACAGTCAAGGCTGAGAATG	ATGGTGGTGAAGACGCCAGTA

2.4. Cell Adhesion Test. BMSCs were cultured in 12-well plates with extracts for 12 h, washed three times with PBS, fixed with 4% paraformaldehyde for 12 min, and permeabilized with 0.1% TritonX-100 for 10 min. The β1-integrin expression was quantitatively assessed via immunofluorescence, with cells blocked with 4% FBS for 30 min and then incubated overnight at room temperature with β1-integrin (Affinity, China) diluted in 1% FBS and Tris-buffered saline. Following three washes with TBST, cells were incubated with goat antirabbit IgG (H + L) Fluor488-conjugated (Affinity, China) for 1 h in the dark. DAPI was then applied for counterstaining in the dark for 5 min, and cells were observed under a fluorescence microscope.

Furthermore, BMSCs were seeded into six-well plates to reach 80% confluence, after which the medium was replaced with a conditioned medium. Next, the expression of FAK and phospho-FAK (p-FAK) protein was analyzed by using a Western blot assay. After 1 and 2 h of incubation, the cells were lysed using protein lysis buffer (Beyotime, China) for 30 min at 4 °C, followed by centrifugation at 12,000 rpm for 20 min. Protein concentrations were determined using a BCA kit (Beyotime, China), separated by 10% SDS-PAGE, and transferred to a poly(vinylidene fluoride) membrane. The membrane was blocked with 5% skim milk and incubated overnight at 4 °C with anti-Phospho-FAK (Tyr397) and FAK antibodies (Thermo Fisher Scientific, USA). Following three washes with Tris-buffered saline, the membrane was further incubated in IRDye 680RD goat antirabbit secondary antibody (Licor, USA) for 2 h at room temperature in the dark. The membrane was scanned with a fluorescence scanner to obtain the image. Western blot band images were quantified using ImageJ software (NIH, USA), with β-actin serving as an internal control.

2.5. Osteogenic Property Test. The osteogenic induction medium was formulated by supplementing the base medium with ascorbic acid (50 nM), dexamethasone (0.1 μM), and β-glyceryl phosphate (10 mM). Various samples were then immersed in this medium to prepare different samples steeped in the osteogenic induction medium. Subsequently, BMSCs were cultured in 24-well plates until they attained 80% confluence, at which point the medium was switched to a conditioned medium to induce differentiation. After 7 days of incubation, the medium was removed and the cells were washed twice with PBS. The qualitative expression of alkaline phosphatase (ALP) in BMSCs was assessed using the BCIP/NBTALP chromogenic kit (Beyotime, China) and the ALP kit (Beyotime, China).

Following the initial seeding in six-well plates, the complete medium was replaced with a conditioned medium after 1 day. Then, 7 days later, cells were harvested for quantitative real-time polymerase chain reaction (RT-qPCR) analysis to measure the expression of bone morphogenic protein 2 (BMP2), runt-related transcription factor 2 (RUNX2), collagen type I (COL-1), and osteocalcin (OCN). mRNA expression levels were quantified using the $2^{-\Delta\Delta Ct}$ method, and the specific primer pairs utilized are listed in Table 2.

2.6. Animal Experiment. The animal experiment received approval from the Experimental Animal Ethics Committee of Affiliated Xinhua Hospital of Dalian University (No. 2021-039-01). Six-month-old rabbits (2.5 kg, Shenyang, China) were randomly divided into three groups: a bare Mg alloy scaffold, an MAO-coated Mg alloy scaffold, and a Ti alloy scaffold group as a control. Anesthesia was administered via an intravenous injection of 3% sodium pentobarbital (30 mg/kg). Under sterile conditions, both forearms of the rabbit were shaved and sterilized, and the bilateral ulnar was exposed by retracting the surrounding muscles.[22] A full-thickness bone defect of 20 mm was created using an oscillating saw under continuous saline irrigation, and the hollow scaffolds were then implanted into the defect. Next, the adjacent soft tissues and muscles were meticulously sutured to stabilize the scaffold. Postoperative care included housing the rabbits in a controlled environment and administering 10 mg/kg subcutaneously for 3 days to prevent infection. Rabbits were permitted to resume normal activities immediately post surgery, including bearing weight on their forearms. Specimens from the forearms of six rabbits were harvested at intervals of 8, 16, and 24 weeks post implantation and subsequently stored at −20 °C for further analysis.

2.7. Radiographic Analysis. The implant degradation and new bone formation were monitored every 4 weeks with a digital X-ray photography system (Rasped Pro80, Shimadzu, Japan) at settings of 110 kV and an anode current of 500 μA. The X-ray images of the ulna defect site were evaluated and scored in three categories: bone formation (0−4), union (0−4), and remodeling (0−4) by three independent investigators based on a previously established standard,[26] with an average of three measurements for each sample. Each category had a possible score ranging from 0 (no healing) to 12 (restoration to normal bone), with a score of 7 considered indicative of preliminary reconstruction.

In order to further evaluate the degradation of the scaffolds, all samples collected at various time points were subjected to high-resolution CT scanning and analysis (Bruker Skyscan 1176, USA). Subsequently, three-dimensional (3D) reconstructions of the defect area were generated from 2D lateral projections using advanced 3D reconstruction software (CTvox). The new bone volume/tissue volume ratio (BV/TV) and CR were then determined through meticulous 3D morphometric analysis.

2.8. Histological Analysis. Bone specimens underwent histological processing to evaluate the microstructure of the newly formed osseous tissue surrounding the scaffolds. In brief, the specimens were immersed in 10% formalin for fixation, followed by triple washes in phosphate-buffered saline (PBS) and decalcification in 10% ethylenediaminetetraacetic acid over an 8-week period. Subsequently, they were embedded in paraffin, sectioned to a thickness of 5 μm, deparaffinized, and rehydrated through a series of graded ethanol solutions. The sections were then stained using hematoxylin and eosin (H&E) as well as the Masson trichrome method (Beyotime, China).

https://doi.org/10.1021/acsomega.4c07635
ACS Omega 2024, 9, 46419−46428

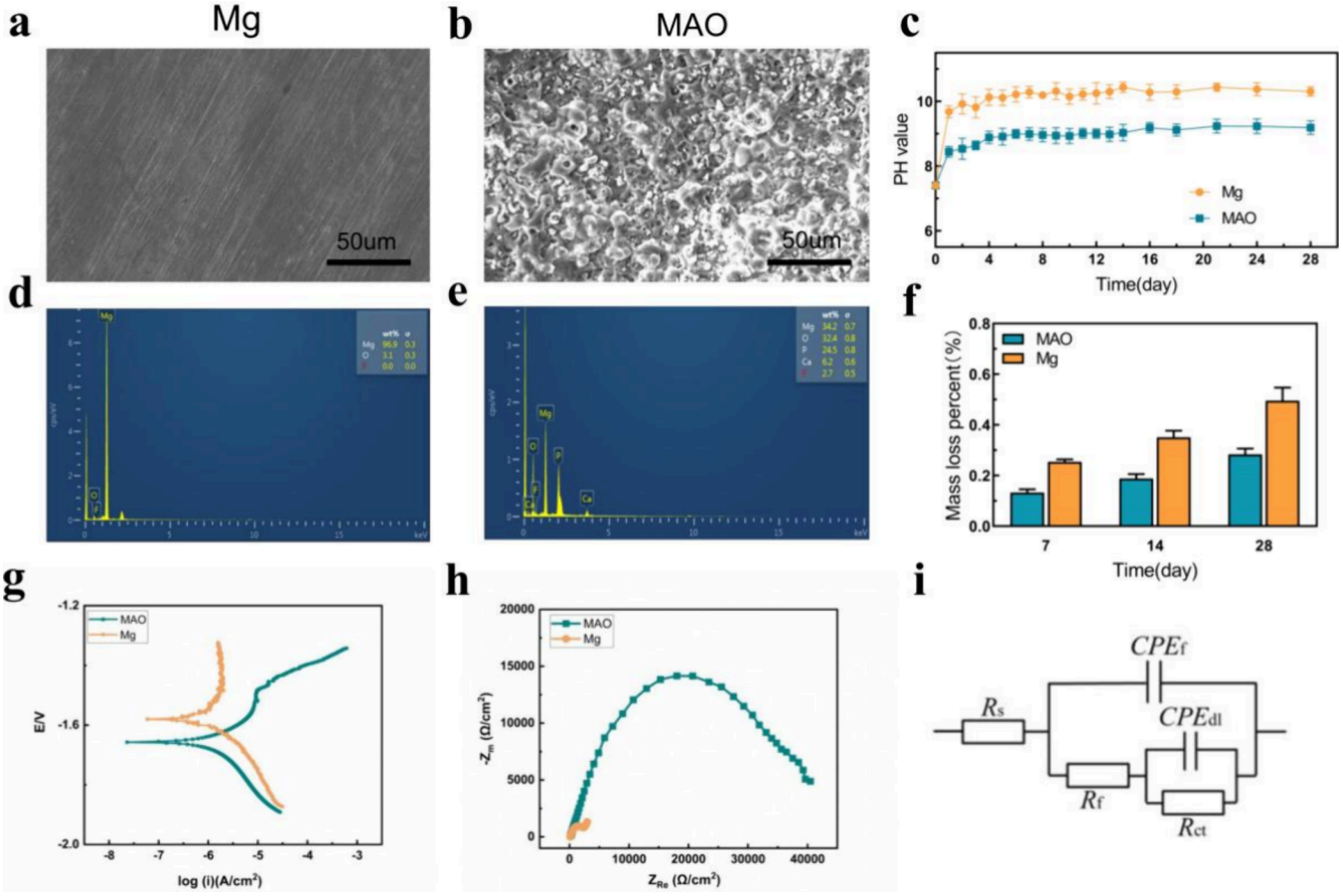

Figure 1. Surface morphology of bare Mg alloy and MAO-coated Mg alloy: (a, b) surface morphologies of bare Mg and MAO-coated Mg alloy; (d, e) EDS results corresponding to (a, b); soaking experiment: (c) pH value; (f) weight loss; electrochemical measurements of bare Mg alloy and MAO-coated Mg alloy: (g) potentiodynamic polarization diagram; (h) Nyquist plot; and (i) equivalent circuit elements.

Table 3. Electrochemical Data from the Nyquist Curve of the Bare Mg Alloy and MAO-Coated Mg Alloy

materials	R_s ($\Omega\cdot cm^2$)	CPEf ($\mu F\cdot cm^{-2}$)	n	R_f ($\Omega\cdot cm^2$)	CP_{Edl} ($\mu F\cdot cm^{-2}$)	n	R_{ct} ($\Omega\cdot cm^2$)
MAO coating	54.72	2.223	0.759	308.2	1.047	0.725	41,510
bare Mg alloy	138.2	34.21	0.732	2906	556.2	0.852	3259

Finally, the stained sections were observed and captured under an optical microscope (Model X71, Olympus, Japan).

2.9. Statistical Analysis. Data were analyzed using SPSS 23.0 software (SPSS Inc., Chicago, IL, USA). Results are presented as mean ± standard deviation. Statistical differences were determined by analysis of variance and Tukey's test, with p values <0.05 deemed statistically significant.

3. RESULTS

3.1. Corrosion Test. In the SEM images, scratches caused by the removal of oxide scale were observed on the bare Mg surface (Figure 1a), while micropores and microcracks were present on the MAO coating (Figure 1b), and some of the micropores were sealed by agglomerates. EDS analysis showed that the elements in the MAO coating were mainly Mg, O, P, and Ca (Figure 1e). Combining the team's previous research and the energy spectrum results, it can be inferred that the main component of the MAO coating is magnesium oxide, and the agglomerates that seal the pores are mainly calcium phosphates.

Electrochemical analyses were carried out to evaluate the degradation in vitro, with the results elegantly depicted in Figure 1g,h. The potentiodynamic polarization revealed that the corrosion potential (E_{corr}) of the uncoated magnesium alloy was approximately −1.596 vs E_{ref} (potential of the reference electrode), which increased to −1.566 vs E_{ref} post MAO treatment (Figure 1g). The potentiodynamic polarization tests showcased a significant reduction in the corrosion current density (I_{corr}) of the MAO-coated magnesium alloy (0.606×10^{-6} A/cm^2) in comparison to the bare alloy (2.201×10^{-6} A/cm^2).

We also used an equivalent circuit to fit the Nyquist curve to further analyze the corrosion principle of the bare Mg alloy and MAO-coated Mg alloy (Figure 1i). Rs is the resistance of the solution. The high-frequency capacitance loop represents the electric double-layer characteristics between the metal and dielectric interface, which is expressed by charge transfer (R_{ct}) and electric double-layer capacity (CP_{Edl}). The medium-frequency capacitance loop represents the correlation between the corrosion product layer and the coating, which is described by the corrosion product layer (R_f) and the corrosion product layer capacity (CP_{Ef}). In Table 3, the R_{ct} (41,510 $\Omega\cdot cm^2$) value of the MAO-coated Ma alloy is significantly higher than that of the bare Mg alloy (3259 $\Omega\cdot cm^2$) alloy, indicating that the charge

https://doi.org/10.1021/acsomega.4c07635
ACS Omega 2024, 9, 46419−46428

transfer of the coated sample is difficult and the corrosion process is effectively inhibited.

Subsequently, a 28-day immersion evaluation was conducted to further examine the long-term corrosion resistance of MAO-coated specimens. As illustrated in Figure 1c, the pH level of the immersion solution for the uncoated magnesium alloy was higher than that of the MAO-coated samples. Moreover, the weight of the specimens exhibited a continuous increase, with the bare alloy registering greater weight loss compared with the coated samples throughout the immersion process (Figure 1f).

3.2. Cytocompatibility. The viability and cytotoxicity of the magnesium alloy coated with MAO were assessed in BMSCs through live/dead staining and the CCK-8 assay, with the titanium alloy employed as the positive control cohort. Fluorescence microscopy unveiled cell viability in diverse sample extracts after a 3-day incubation period (Figure 2a).

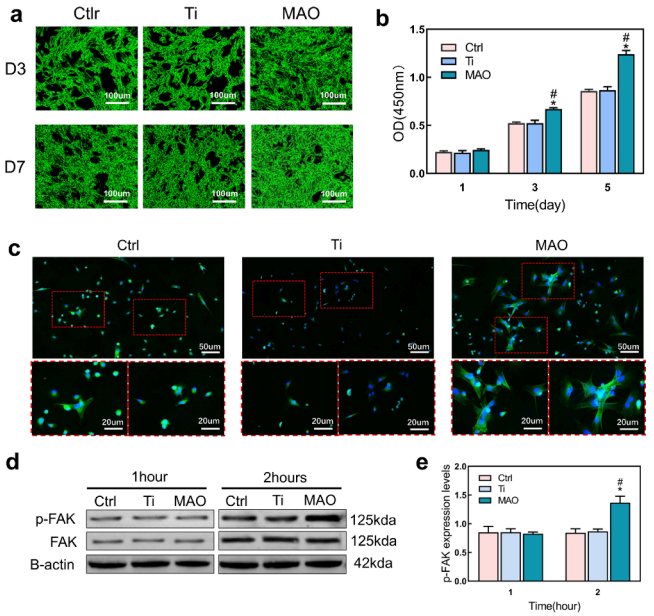

Figure 2. Cell viability of BMSCs after incubation with extracts from different culture media (control, Ti, and MAO-coated Mg alloy). (a) Live−dead staining fluorescence images after coculture of extracts with BMSCs for 3 and 7 days, with live cells in green and dead cells in red. (b) CCK-8 detection of extracts cocultured with BMSCs for 1, 3, and 5 days. (c) Immunofluorescence images showing the expression of integrin β1 in BMSCs after treatment with different extracts. (d) Western blotting of FAK and p-FAK. (e) Corresponding quantification of Western blots (# and * indicate $p < 0.05$ for the MAO-coated Mg alloy compared with the negative control and Ti, respectively).

Simultaneously, the CCK-8 outcomes indicated a surge in the optical density (OD) values of BMSCs on days 3 and 5 (Figure 2b). Notably, in comparison to both the control and titanium alloy groups, the MAO-coated magnesium alloy exhibited elevated OD values and accelerated growth kinetics.

To assess the impact of MAO-coated magnesium alloy on cell adhesion, extracts from different experimental groups were cocultured with BMSCs for a duration of 12 h, followed by analysis of β1-integrin expression. Two-color in situ fluorescence imaging revealed that cells cocultured with extracts from the MAO-coated magnesium alloy group exhibited robust cell spreading, as well as elevated expression and a broader distribution of β1-integrin compared to cells in the control and titanium groups (Figure 2c). Additionally, the expression levels of phosphorylated focal adhesion kinase (p-FAK) were evaluated qualitatively and quantitatively through Western blot analysis (Figure 2d) and RT-qPCR (Figure 2e). No significant differences in p-FAK levels were observed after 1 h of coculture among the three groups. However, after 2 h, the expression level of p-FAK was significantly higher in the MAO-coated magnesium alloy group compared to the other groups.

3.3. Osteogenic Properties. ALP levels, a preliminary indicator of the differentiation of BMSCs into osteoblasts, were used to determine whether the scaffold promoted osteogenesis. Figure 3a,b show that after 3 and 7 days of induction BMSCs cultured with the MAO-coated Mg alloy extract exhibited markedly deeper staining and higher ALP activity compared to the other two groups. The osteogenic potential of BMSCs after 7 days of culture was further confirmed using RT-qPCR to measure the expression levels of osteogenesis-related genes (BMP2, RUNX2, COL-1, and OCN), with the results displayed in Figure 3c−f, respectively. Among them, the expression levels of osteogenesis-related genes were the highest in the MAO-coated Mg alloy group.

The ALP levels, serving as a preliminary indicator of bone marrow-derived mesenchymal stem cell differentiation into osteoblasts,[31] were utilized to assess the scaffold's ability to promote osteogenesis. As shown in Figure 3a,b, BMSCs cultured with the MAO-coated Mg alloy extract exhibited significantly deeper staining and increased ALP activity after 3 and 7 days of induction, surpassing those of the other two experimental groups. Furthermore, the osteogenic potential of BMSCs following 7 days of culture was confirmed through RT-qPCR analysis of osteogenesis-related gene expression levels, including BMP2, RUNX2, COL-1, and OCN, as shown in Figure 3c−f, respectively. Notably, the MAO-coated Mg alloy group demonstrated the highest expression levels of osteogenesis-related genes.

3.4. X-ray. Figure 4a illustrates the general appearance of scaffolds (comprising titanium alloy, bare Mg alloy, and MAO-coated Mg alloy) prior to surgical intervention, while Figure 4b elucidates a surgical schematic of a 20 mm ulna large segment bone defect rectified employing an MAO-coated scaffold. The degeneration of these scaffolds was tracked post surgery through X-ray imaging. Initially, shadowy regions suggestive of excessive hydrogen were discerned surrounding the bare Mg alloy scaffold and the MAO-coated scaffold at 8 weeks post surgery (Figure 4c). Subsequently, these shadowy areas dissipated around the MAO-coated scaffold by the 16- and 24-week marks post surgery. Concurrently, the silhouette of the MAO-coated scaffold remained sharp, in stark contrast to the gradual degradation and fading visibility of the bare Mg alloy scaffold (Figure 4d,e).

In the interim, the novel bone regeneration process underwent quantitative evaluation through X-ray analysis, and the findings are elegantly portrayed in Figure 4f. As the study progressed, at the 8-week mark, the X-ray assessments revealed values of 0.28 ± 0.08 for the titanium alloy scaffold group, 1.22 ± 0.34 for the bare Mg scaffold group, and an impressive 3.61 ± 0.21 for the Mg alloy scaffold group with MAO coating. Regarding the 16-week milestone, the X-ray evaluations displayed a notable escalation to 7.78 ± 0.34 within the MAO-coated magnesium scaffold group, whereas the scores for the titanium alloy scaffold group (0.67 ± 0.36) and the unmodified magnesium scaffold group (0.38 ± 0.21) remained relatively constant. Upon reaching the 24-week juncture, the X-ray scores reflected values of 0.44 ± 0.21 for the titanium alloy

https://doi.org/10.1021/acsomega.4c07635
ACS Omega 2024, 9, 46419−46428

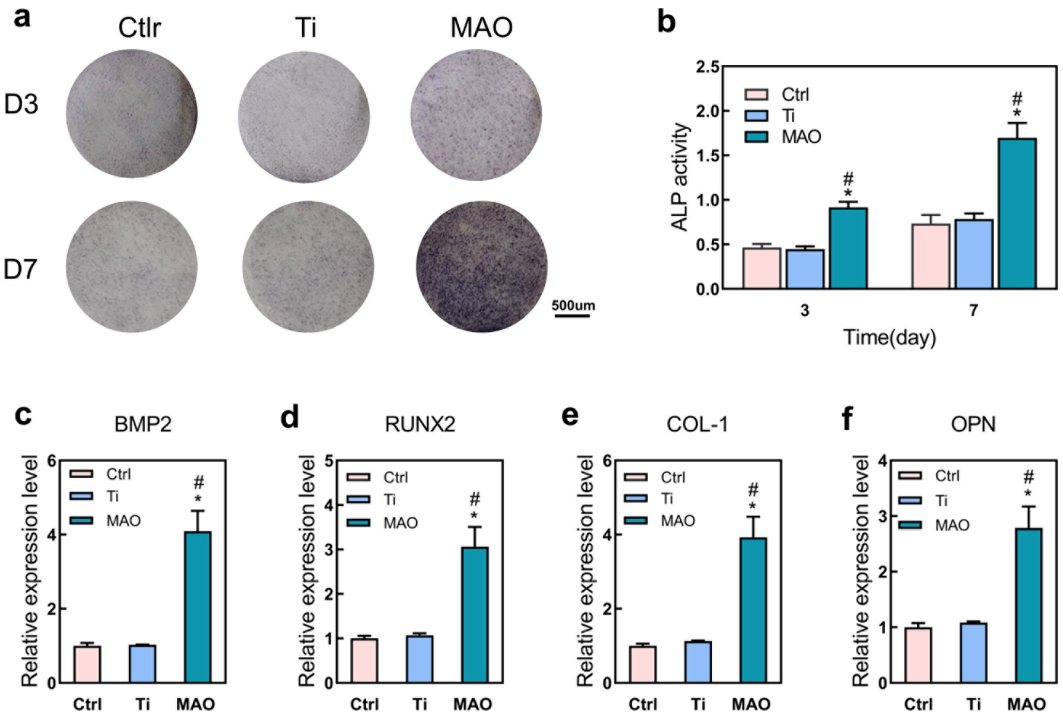

Figure 3. Detection of the osteogenic ability of BMSCs after incubation with different sample extracts (control, Ti, and MAO-coated Mg alloy): (a) ALP staining; (b) ALP activity; (c–f) gene expression of BMP2, RUN2, COL-1, and OCN levels (# and * indicate $p < 0.05$ for the MAO-coated Mg alloy compared with the negative control and Ti, respectively).

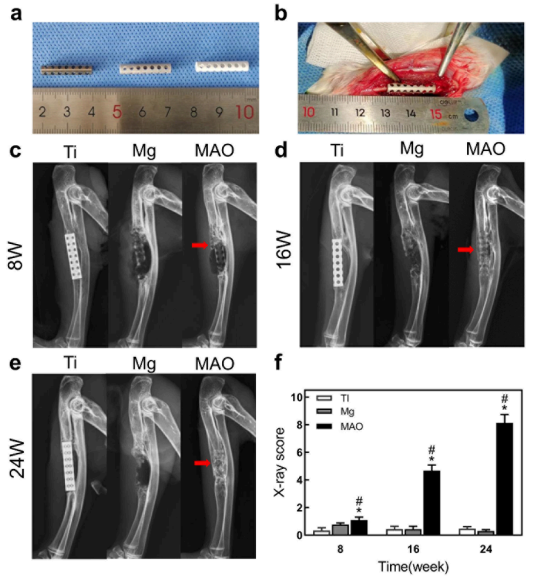

Figure 4. (a) Ti, bare Mg scaffold, and MAO-coated Mg scaffold. (b) Scaffold implanted into a large segmental bone defect of rabbit ulna (20 mm). (c–e) X-ray images of rabbit ulna at 8, 16, and 24 weeks after surgery. The red arrow indicates bone formation. (f) X-ray radiography score (# and * indicate $p < 0.05$ for the MAO-coated Mg scaffold compared with Ti and bare Mg scaffold, respectively).

scaffold group and 0.39 ± 0.16 for the bare Mg scaffold group, while the MAO-coated Mg scaffold group demonstrated a remarkable score of 10.39 ± 0.34.

3.5. Micro-CT. Further assessments of bone tissue regeneration and degradation of scaffolds were performed using 3D Micro-CT, with findings depicted in Figure 5. At 8 weeks post surgery, significant degradation was observed in the bare Mg scaffold in comparison to both the MAO-coated Mg scaffold and Ti scaffold, with minimal new callus formation noted on the surface and around the implants (Figure 5a). With time, the MAO-coated Mg scaffold demonstrated sustained structural integrity, while most of the structure of the bare Mg scaffold exhibited extensive degradation by 16 and 24 weeks (Figure 5b). Additionally, a higher prevalence of new bone callus formation was observed around the MAO-coated Mg scaffold compared to the other two groups. Figure 5c reveals that the BV/TV ratio, as determined by Micro-CT, was consistently higher in the MAO-coated scaffold group than in the Ti and bare Mg scaffold groups at all time points. Furthermore, the corrosion rate (CR) of the scaffolds, calculated and shown in Figure 5d, indicated initial rates of 0.46 ± 0.04 mm/year for the bare Mg alloy scaffold and 0.18 ± 0.04 mm/year for the MAO-coated Mg scaffold at 8 weeks post surgery. As the study progressed, the CR of the bare Mg alloy scaffold remained at 0.46 ± 0.02 mm/year at 16 weeks and reduced to 0.33 ± 0.01 mm/year by 24 weeks, whereas the CR of the MAO-coated Mg scaffold remained stable at 0.22 ± 0.02 and 0.22 ± 0.01 mm/year at both 16 and 24 weeks.

3.6. Histology. Figure 6 presents the histological representations of the new bone tissue formations utilizing both H&E and Masson staining tests on the peripheries of the scaffolds at weeks 8, 16, and 24. The unmarked area denotes the site of graft excision. The Ti alloy scaffold group exhibited more mature bone, with negligible new bone growth detected in the space between the implant and the ulna. In contrast, the bare Mg alloy group displayed a marked increase in collagen deposition and bone formation by the eighth week, followed by a gradual decline. The MAO-coated magnesium alloy group showed an incremental rise in the number of collagen fibers and stained areas during various stages of bone repair. Meanwhile, the Masson staining revealed a predominance of blue-stained

https://doi.org/10.1021/acsomega.4c07635
ACS Omega 2024, 9, 46419−46428

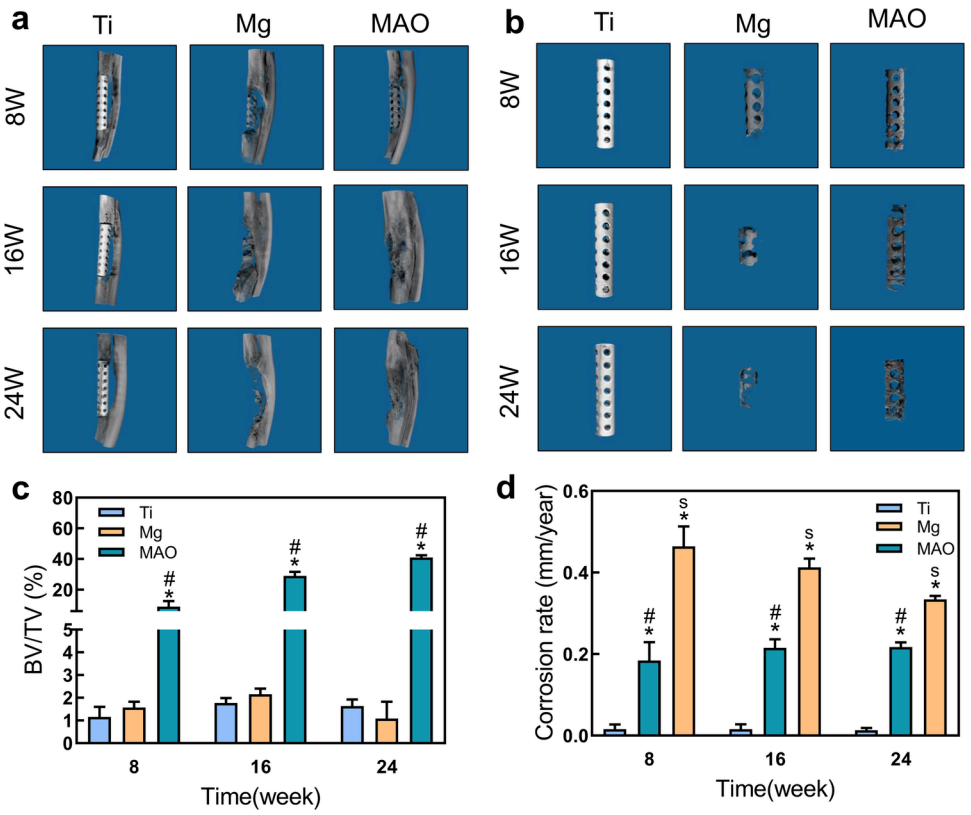

Figure 5. 3D reconstructed images of rabbit ulna at 8, 16, and 24 weeks in Ti, bare Mg scaffold, and MAO-coated Mg scaffold obtained by Micro-CT measurement. (a) Bone defect; (b) scaffold; (c) BV/TV; and (d) CR (# and * indicate $p < 0.05$ for the MAO-coated Mg scaffold compared with Ti and the bare Mg scaffold, respectively; s indicates $p < 0.01$ for the bare Mg scaffold compared with Ti).

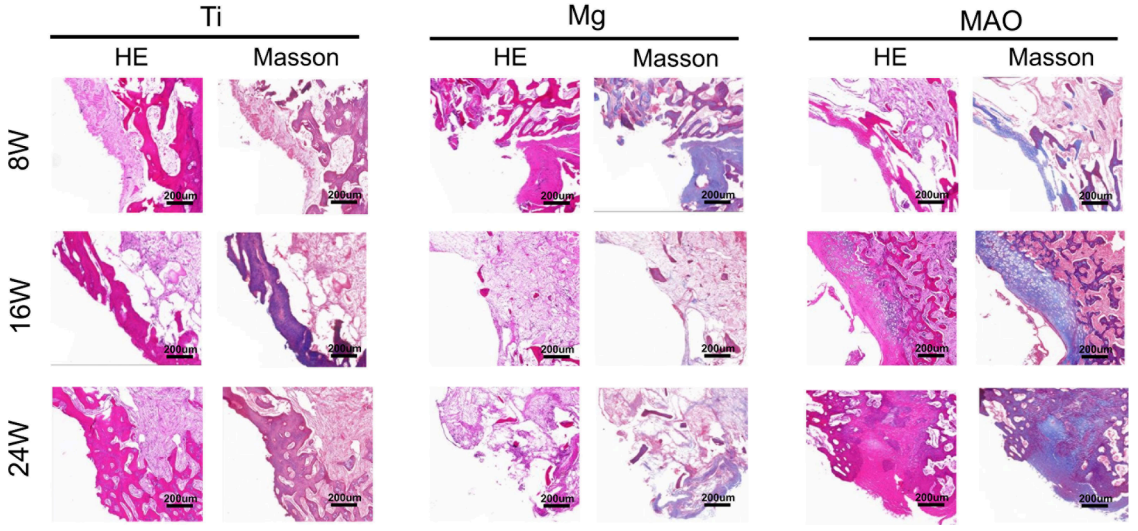

Figure 6. Representative images of HE staining and Masson's trichrome staining of the interface between the scaffold and bone after different implantation periods. Collagen fibers and chondrocytes, blue staining; immature bone tissue, red-blue staining; mature bone, red staining.

cartilaginous tissues and cells in the newly formed tissues surrounding the bare Mg scaffold group at 8 weeks after surgery. However, at 16 and 24 weeks, an increased presence of blue-dyed cartilage tissues and cells was noted around the MAO-coated Mg scaffold group compared to the other two groups.

4. DISCUSSION

The pursuit of an optimal orthopedic implant material for bone defect repair has intensified over the last two decades, yet a satisfactory alternative has not emerged. This is primarily due to the intricate internal dynamics of critical-size bone defects, such as defect dimensions, local vascularization, susceptibility to infection, and soft tissue integration, which impose heightened demands on the osteogenic properties of implant materials.[32] Our preliminary studies have shown that the utilization of magnesium (Mg) alloy scaffolds in conjunction with autogenous bone grafting is efficacious in the remediation of profound bone deficiencies.[18,25,26] However, the intrinsic osteogenic potential

https://doi.org/10.1021/acsomega.4c07635
ACS Omega 2024, 9, 46419−46428

of Mg alloy scaffolds, independent of autogenous bone, remains uncertain. Therefore, this research employed a Mg−Zn−Nd−Zr alloy as a substrate for scaffold fabrication, enhancing its degradation rate and biocompatibility through a self-sealing MAO coating enriched with calcium and phosphorus.[33] The empty scaffold was implanted into a 20 mm ulna bone defect in the rabbit model. To our knowledge, this represents the initial investigation into the osteogenic effect of the Mg alloy itself in large segmental bone defects, which aids in the elucidation of its corrosion resistance, osteoconduction, and osteoinductivity within the challenging milieu of a bone defect.

As widely acknowledged, MAO is a viable method for creating corrosion-resistant coatings on magnesium alloys. These coatings are characterized by their strong metallurgical bonding strength, excellent biocompatibility, and resistance to corrosion of the substrate.[34−36] In the present study, electrochemical assessments indicated that the MAO coating markedly elevated the E_{corr} value and R_{ct}, reducing the I_{corr} value of the bare Mg alloy, thereby augmenting its resistance to corrosion. In this study, a 28-day long-term immersion test revealed that the weight loss of the untreated Mg alloy was higher than that of the coated samples throughout the immersion process. These findings strongly indicate a substantial improvement in the corrosion resistance of the Mg alloy substrate material following the coating treatment, a conclusion indirectly supported by the changes in the pH value of the immersion solution. In addition, the released Mg^{2+} from the corrosion of the Mg alloy can produce biological effects, such as local pH value fluctuations and potential cytotoxicity.[37,38] The MAO coatings can play a role in the sustained release of magnesium ions, thereby reducing potential cytotoxicity and increasing its biological activity. At last, X-ray images have confirmed the structural integrity of the titanium alloy scaffold in vivo. While the bare Mg alloy scaffold rapidly degraded, completely disintegrating by 16 weeks, the presence of the MAO coating on the Mg alloy scaffold allowed it to maintain its structural integrity for up to 24 weeks after implantation. Furthermore, Micro-CT results revealed that the CR of the bare Mg scaffold peaked at 8 weeks post surgery and then decreased over time, likely due to the rapid degradation of the bare Mg alloy scaffolds in the early stages. In contrast, the CR of the MAO-coated Mg scaffold group remained stable after surgery, highlighting the efficacy of the MAO coating in enhancing corrosion resistance and prolonging the mechanical properties under complex internal environments. In summary, our results confirmed that MAO coating can effectively inhibit the corrosion behavior of the magnesium alloy matrix both in vitro and in vivo, which helps Mg alloy scaffolds play a supporting and fixing role in repairing bone defects.

However, the principal role of orthopedic implants in repairing bone defects goes beyond providing mechanical and structural support; they must also convey biological signals to cells in a specific manner to enhance bone growth.[39] Thus, simply having corrosion resistance is inadequate for the MAO coating of Mg alloy scaffolds; their osteogenic properties, such as osteoinduction and osteoconduction, are equally crucial. Numerous studies have demonstrated that magnesium ions released during the degradation of the Mg alloy significantly activate integrins signaling[40] and FAK pathways,[41] prompting nearby prebone cells to differentiate into bone cells. In this study, we observed that the β1-integrin protein and the p-FAK were highly expressed in the BMSCs cocultured with MAO-coated samples. Simultaneously, there was a notable increase in the ALP activity and expression of osteogenesis-related genes, such as BMP2, RUNX2, COL-1, and OCN, in the BMSCs. These findings indicate that the MAO-coated Mg alloy exhibits robust bone induction in vitro. In the subsequent implantation experiment, histological analyses revealed a prevalence of blue-dyed fibrous tissues and chondrocytes around bare magnesium scaffolds at 8 weeks post surgery. It was observed that new bone tissues appeared to be more mature, indicating a heightened osteogenic response in the bare Mg alloy scaffold group in comparison to the other two groups. Interestingly, by 16 and 24 weeks post surgery, this phenomenon waned in the unadorned magnesium alloy group, while increasing amounts of mature bone tissue and azure-dyed cartilage tissues were observed in the vicinity of the MAO-coated Mg scaffold group. We hypothesize that this pattern may be ascribed to the release of Mg^{2+} brought about by varying rates of degradation in the scaffolds. At the age of 8 weeks, the swift breakdown of the bare Mg alloy scaffolds resulted in the substantial release of magnesium ions, thereby intensifying a powerful bone formation response among nearby bone precursor cells. However, as the breakdown of the scaffolds continued, the released magnesium ions gradually diminished along with their stimulating capacity. In contrast, the MAO-coated Mg alloy scaffold maintained a consistent breakdown rate, continuously releasing magnesium ions and maintaining a strong bone renewal response, underscoring their effective stimulating capacity in living organisms.

In addition to osteoinduction, osteoconduction is another crucial characteristic of magnesium alloy scaffolds in the process of bone defect reconstruction, defined as "enabling the infiltration or proliferation of bone cells along the surface of the scaffold, provided there is direct contact with living bone at one or both extremities".[42] However, the focus on osteoinduction and stem cell applications in bone tissue engineering has overshadowed the significance of osteoconduction as a major contributor to bone regeneration. Our study findings reaffirmed that the β1-integrin protein and the p-FAK were highly expressed in the BMSCs cocultured with MAO-coated samples, highlighting the efficacy of the samples in promoting cell adhesion and facilitating osteoblast migration and proliferation on the sample's surface. More importantly, through the X-ray and Micro-CT images during implantation trials, we clearly visualized the progressive substitution of new bone formation on the surface of the MAO-coated Mg alloy scaffold. After 8 weeks, new bone regeneration was evident at the site of the MAO-coated scaffold and the broken end of the bone. By 16 weeks, the new bone tissue had extended along the surface of the scaffold from both ends to the center, ultimately culminating in the formation of bone-bridging tissue at 24 weeks. Interestingly, similar phenomena were absent on the surfaces of the titanium alloy scaffold and the bare magnesium alloy scaffold, where new bone formation was limited to the ends of the scaffold. This difference may result from the rapid degradation rate of bare Mg alloy scaffolds, leading to rapid structural loss that loses the necessary support for new bone formation. Additionally, while titanium alloy scaffolds could provide ample structural support, they lack inherent bone inductive properties and are devoid of the cytokines necessary for activating new bone regeneration without supplementary bone graft materials. This deficiency ultimately results in a reparative failure. Therefore, our results not only confirmed for the first time that the Mg alloy scaffold itself has good osteoconductivity to induce new bone to crawl on its surface but also demonstrated once again that it is necessary to provide support for new bone regeneration at the site of bone defect.

https://doi.org/10.1021/acsomega.4c07635
ACS Omega 2024, 9, 46419−46428

To sum up, despite certain limitations, such as unaddressed local air accumulation and the absence of in vivo data from larger animals such as goats and assessment of the mechanical properties of the repaired ulna, our study substantiates the integral roles of both osteoconduction and osteoinduction of the implant material itself in reconstructing substantial bone defects without additional bone graft materials. This suggests that when developing new implant materials in the future, concentrating solely on only one of these aspects may prove insufficient.

5. CONCLUSIONS

In this research, an MAO-coated magnesium alloy scaffold demonstrating excellent osteoinductivity and osteoconductivity was devised and successfully used to repair extensive segmental bone defects in rabbit ulna without the need for external bioactive factors, cells, or autologous particulate bone. This study provides an experimental basis for further understanding the inherent characteristics of bioactive magnesium alloy scaffolds in the process of reconstructing large bone defects and also offers a promising alternative material and a new approach for the clinical treatment of large bone defects.

AUTHOR INFORMATION

Corresponding Author

Nan Zhang − *Department of Orthopaedics, Affiliated Xinhua Hospital of Dalian University, Dalian 116001, China;* Present Address: No 156, Wansui street, Shahekou District, Dalian, Liiaoning, China; orcid.org/0000-0002-6441-8022; Email: zhn1979-08@163.com

Authors

Shujun Liu − *Department of Orthopaedics, Affiliated Xinhua Hospital of Dalian University, Dalian 116001, China*

Ming Gao − *Institute of Metal Research, Chinese Academy of Sciences, Shenyang 110016, China*

Na Liu − *Department of Orthopaedics, Affiliated Xinhua Hospital of Dalian University, Dalian 116001, China*

Ruixin Li − *Department of Orthopaedics, Affiliated Xinhua Hospital of Dalian University, Dalian 116001, China*

Zhiyong Zhang − *Department of Orthopaedics, Affiliated Xinhua Hospital of Dalian University, Dalian 116001, China*

Yuan Yao − *Department of Orthopaedics, Affiliated Xinhua Hospital of Dalian University, Dalian 116001, China*

Weiming Wang − *Department of Orthopaedics, Affiliated Xinhua Hospital of Dalian University, Dalian 116001, China*

Lili Tan − *Institute of Metal Research, Chinese Academy of Sciences, Shenyang 110016, China*

Complete contact information is available at: https://pubs.acs.org/10.1021/acsomega.4c07635

Author Contributions

S.L.: writing—original draft, project administration, investigation, data curation, conceptualization; M.G.: writing—original draft, investigation, data curation, conceptualization; N.L.: investigation; R.L.: investigation; Z.Z.: methodology; Y.Y.: investigation; W.W.: resources, funding acquisition; L.T.: funding acquisition, conceptualization, project administration; N.Z.: funding acquisition, conceptualization, resources, project administration, writing—review and editing.

Notes

The authors declare no competing financial interest.

ACKNOWLEDGMENTS

This work was financially supported by funds from the Key Discipline Project of Affiliated Xinhua Hospital of Dalian University (2022003, N.Z.), the Interdisciplinary Project of Dalian University (DLUXK-2023-YB-008, N.Z.), and the Basic Applied Research Program of Liaoning Province of China (No. 2022020347-JH2/1013, L.T.).

REFERENCES

(1) Zhao, Q.; Ni, Y.; Wei, H.; Duan, Y.; Chen, J.; Xiao, Q.; Gao, J.; Yu, Y.; Cui, Y.; Ouyang, S.; Miron, R. J.; Zhang, Y.; Wu, C. Ion incorporation into bone grafting materials. *Periodontology 2000* **2024**, *94*, 213−230.

(2) Zhou, B.; Jiang, X.; Zhou, X.; Tan, W.; Luo, H.; Lei, S.; Yang, Y. GelMA-based bioactive hydrogel scaffolds with multiple bone defect repair functions: therapeutic strategies and recent advances. *Biomater Res.* **2023**, *27* (1), 86.

(3) Wang, Y.; Li, M.; Li, P.; Teng, H.; Fan, D.; Du, W.; Guo, Z. Progress and Applications of Polyphosphate in Bone and Cartilage Regeneration. *Biomed. Res. Int.* **2019**, *2019*, No. 5141204.

(4) Zhang, Y.; Wu, D.; Zhao, X.; Pakvasa, M.; Tucker, A. B.; Luo, H.; Qin, K. H.; Hu, D. A.; Wang, E. J.; Li, A. J.; Zhang, M.; Mao, Y.; Sabharwal, M.; He, F.; Niu, C.; Wang, H.; Huang, L.; Shi, D.; Liu, Q.; Ni, N.; Fu, K.; Chen, C.; Wagstaff, W.; Reid, R. R.; Athiviraham, A.; Ho, S.; Lee, M. J.; Hynes, K.; Strelzow, J.; He, T. C.; El Dafrawy, M. Stem Cell-Friendly Scaffold Biomaterials: Applications for Bone Tissue Engineering and Regenerative Medicine. *Front Bioeng Biotechnol.* **2020**, *8*, No. 598607.

(5) Schmidt, A. H. Autologous bone graft: Is it still the gold standard? *Injury* **2021**, *52* (Suppl 2), S18−S22.

(6) Sharifi, M.; Kheradmandi, R.; Salehi, M.; Alizadeh, M.; Ten Hagen, T. L. M.; Falahati, M. Criteria, Challenges, and Opportunities for Acellularized Allogeneic/Xenogeneic Bone Grafts in Bone Repairing. *ACS Biomater Sci. Eng.* **2022**, *8* (8), 3199−3219.

(7) Wang, X.; Xu, S.; Zhou, S.; Xu, W.; Leary, M.; Choong, P.; Qian, M.; Brandt, M.; Xie, Y. M. Topological design and additive manufacturing of porous metals for bone scaffolds and orthopaedic implants: A review. *Biomaterials.* **2016**, *83*, 127−141.

(8) Spriano, S.; Yamaguchi, S.; Baino, F.; Ferraris, S. A critical review of multifunctional titanium surfaces: New frontiers for improving osseointegration and host response, avoiding bacteria contamination. *Acta Biomater.* **2018**, *79*, 1−22.

(9) Bai, L.; Du, Z.; Du, J.; Yao, W.; Zhang, J.; Weng, Z.; Liu, S.; Zhao, Y.; Liu, Y.; Zhang, X.; Huang, X.; Yao, X.; Crawford, R.; Hang, R.; Huang, D.; Tang, B.; Xiao, Y. A multifaceted coating on titanium dictates osteoimmunomodulation and osteo/angio-genesis towards ameliorative osseointegration. *Biomaterials.* **2018**, *162*, 154−169.

(10) Li, D.; Dai, D.; Xiong, G.; Lan, S.; Zhang, C. Composite Nanocoatings of Biomedical Magnesium Alloy Implants: Advantages, Mechanisms, and Design Strategies. *Adv. Sci.* **2023**, *10* (18), No. 2300658.

(11) Zhang, T.; Wang, W.; Liu, J.; Wang, L.; Tang, Y.; Wang, K. A review on magnesium alloys for biomedical applications. *Front Bioeng Biotechnol.* **2022**, *10*, No. 953344.

(12) Wang, J. L.; Xu, J. K.; Hopkins, C.; Chow, D. H.; Qin, L. Biodegradable Magnesium-Based Implants in Orthopedics-A General Review and Perspectives. *Adv. Sci.* **2020**, *7* (8), No. 1902443.

(13) Witte, F. The history of biodegradable magnesium implants: a review. *Acta Biomater.* **2010**, *6* (5), 1680−1692.

(14) Chen, L.; Yan, Z.; Qiu, T.; Zhu, J.; Liu, G.; Han, J.; Guo, C. Long-Term Temporospatial Complementary Relationship between Degradation and Bone Regeneration of Mg-Al Alloy. *ACS Appl. Bio Mater.* **2023**, *6* (11), 4703−4713.

(15) Jian, S. Y.; Lin, C. F.; Tsai, T. L.; Wang, P. H.; Chen, C. H.; Lin, S. Y.; Tseng, C. C. In Vivo Degradation Behavior of Magnesium Alloy for Bone Implants with Improving Biological Activity, Mechanical Properties, and Corrosion Resistance. *Int. J. Mol. Sci.* **2023**, *24* (2), 1602.

(16) Wang, W.; Nune, K. C.; Tan, L.; Zhang, N.; Dong, J.; Yan, J.; Misra, R. D. K.; Yang, K. Bone regeneration of hollow tubular magnesium-strontium scaffolds in critical-size segmental defects: Effect of surface coatings. *Mater. Sci. Eng. C Mater. Biol. Appl.* **2019**, *100*, 297−307.
(17) Xi, Z.; Wu, Y.; Xiang, S.; Sun, C.; Wang, Y.; Yu, H.; Fu, Y.; Wang, X.; Yan, J.; Zhao, D.; Wang, Y.; Zhang, N. Corrosion Resistance and Biocompatibility Assessment of a Biodegradable Hydrothermal-Coated Mg-Zn-Ca Alloy: An in Vitro and in Vivo Study. *ACS Omega.* **2020**, *5* (9), 4548−4557.
(18) Sun, H.; Wang, Y.; Sun, C.; Yu, H.; Xi, Z.; Liu, N.; Zhang, N. In vivo comparison of the degradation and osteointegration properties of micro-arc oxidation-coated Mg-Sr and Mg-Ca alloy scaffolds. *Biomed Mater. Eng.* **2022**, *33* (3), 209−219.
(19) Zhao, D.; Huang, S.; Lu, F.; Wang, B.; Yang, L.; Qin, L.; Yang, K.; Li, Y.; Li, W.; Wang, W.; Tian, S.; Zhang, X.; Gao, W.; Wang, Z.; Zhang, Y.; Xie, X.; Wang, J.; Li, J. Vascularized bone grafting fixed by biodegradable magnesium screw for treating osteonecrosis of the femoral head. *Biomaterials.* **2016**, *81*, 84−92.
(20) Wang, T.; Ni, G.; Furushima, T.; Diao, H.; Zhang, P.; Chen, S.; Fogarty, C. E.; Jiang, Z.; Liu, X.; Li, H. Mg alloy surface immobilised with caerin peptides acquires enhanced antibacterial ability and putatively improved corrosion resistance. *Mater. Sci. Eng. C Mater. Biol. Appl.* **2021**, *121*, No. 111819.
(21) Windhagen, H.; Radtke, K.; Weizbauer, A.; Diekmann, J.; Noll, Y.; Kreimeyer, U.; Schavan, R.; Stukenborg-Colsman, C.; Waizy, H. Biodegradable magnesium-based screw clinically equivalent to titanium screw in hallux valgus surgery: short term results of the first prospective, randomized, controlled clinical pilot study. *Biomed. Eng. Online* **2013**, *12*, 62.
(22) Lee, J. W.; Han, H. S.; Han, K. J.; Park, J.; Jeon, H.; Ok, M. R.; Seok, H. K.; Ahn, J. P.; Lee, K. E.; Lee, D. H.; Yang, S. J.; Cho, S. Y.; Cha, P. R.; Kwon, H.; Nam, T. H.; Han, J. H.; Rho, H. J.; Lee, K. S.; Kim, Y. C.; Mantovani, D. Long-term clinical study and multiscale analysis of in vivo biodegradation mechanism of Mg alloy. *Proc. Natl. Acad. Sci. U. S. A.* **2016**, *113* (3), 716−721.
(23) Xie, K.; Wang, L.; Guo, Y.; Zhao, S.; Yang, Y.; Dong, D.; Ding, W.; Dai, K.; Gong, W.; Yuan, G.; Hao, Y. Effectiveness and safety of biodegradable Mg-Nd-Zn-Zr alloy screws for the treatment of medial malleolar fractures. *J. Orthop Translat.* **2021**, *27*, 96−100.
(24) Smith, M. R.; Atkinson, P.; White, D.; Piersma, T.; Gutierrez, G.; Rossini, G.; Desai, S.; Wellinghoff, S.; Yu, H.; Cheng, X. Design and assessment of a wrapped cylindrical Ca-P AZ31 Mg alloy for critical-size ulna defect repair. *J. Biomed Mater. Res. B: Appl. Biomater.* **2012**, *100* (1), 206−216.
(25) Zhang, N.; Zhao, D.; Liu, N.; Wu, Y.; Yang, J.; Wang, Y.; Xie, H.; Ji, Y.; Zhou, C.; Zhuang, J.; Wang, Y.; Yan, J. Assessment of the degradation rates and effectiveness of different coated Mg-Zn-Ca alloy scaffolds for in vivo repair of critical-size bone defects. *J. Mater. Sci. Mater. Med.* **2018**, *29* (9), 138.
(26) Zhang, N.; Wang, W.; Zhang, X.; Nune, K. C.; Zhao, Y.; Liu, N.; Misra, R. D. K.; Yang, K.; Tan, L.; Yan, J. The effect of different coatings on bone response and degradation behavior of porous magnesium-strontium devices in segmental defect regeneration. *Bioact Mater.* **2021**, *6* (6), 1765−1776.
(27) Miron, R. J.; Zhang, Y. F. osteoinduction: a review of old concepts with new standards. *J. Dent Res.* **2012**, *91* (8), 736−744.
(28) Albrektsson, T.; Johansson, C. Osteoinduction, osteoconduction and osseointegration. *Eur. Spine J.* **2001**, *10* (Suppl 2), S96−S101.
(29) Testing, A.S.f. and Materials. *ASTM G31−72: Standard Practice for Laboratory Immersion Corrosion Testing of Metals*; ASTM, 2004.
(30) De Jong, W.; Carraway, J.; Geertsma, R. In vivo and in vitro testing for the biological safety evaluation of biomaterials and medical devices. In *Biocompatibility and Performance of Medical Devices*; Elsevier, 2020; pp 123−166.
(31) Kikyo, N. Circadian Regulation of Bone Remodeling. *Int. J. Mol. Sci.* **2024**, *25* (9), 4717.
(32) Witek, L.; Alifarag, A. M.; Tovar, N.; Lopez, C. D.; Cronstein, B. N.; Rodriguez, E. D.; Coelho, P. G. Repair of Critical-Sized Long Bone Defects Using Dipyridamole-Augmented 3D-Printed Bioactive Ceramic Scaffolds. *J. Orthop Res.* **2019**, *37* (12), 2499−2507.
(33) Chen, J.; Zhang, Y.; Ibrahim, M.; Etim, I. P.; Tan, L.; Yang, K. In vitro degradation and antibacterial property of a copper-containing micro-arc oxidation coating on Mg-2Zn-1Gd-0.5Zr alloy. *Colloids Surf. B Biointerfaces.* **2019**, *179*, 77−86.
(34) Daroonparvar, M.; Yajid, M. A. M.; Yusof, N. M.; Bakhsheshi-Rad, H. R.; Hamzah, E.; Mardanikivi, T. Deposition of duplex MAO layer/nanostructured titanium dioxide composite coatings on Mg−1% Ca alloy using a combined technique of air plasma spraying and micro arc oxidation. *J. Alloys Compd.* **2015**, *649*, 591−605.
(35) Bakhsheshi-Rad, H. R.; Hamzah, E.; Ebrahimi-Kahrizsangi, R.; Daroonparvar, M.; Medraj, M. Fabrication and characterization of hydrophobic microarc oxidation/poly-lactic acid duplex coating on biodegradable Mg−Ca alloy for corrosion protection. *Vacuum* **2016**, *125*, 185−188.
(36) Wu, Y.; Wang, Y. M.; Zhao, D. W.; Zhang, N.; Li, H.; Li, J.; Wang, Y.; Zhao, Y.; Yan, J.; Zhou, Y. In vivo study of microarc oxidation coated Mg alloy as a substitute for bone defect repairing: Degradation behavior, mechanical properties, and bone response. *Colloids Surf. B Biointerfaces.* **2019**, *181*, 349−359.
(37) (37.) Butt, M. S.; Maqbool, A.; Saleem, M.; Umer, M. A.; Javaid, F.; Malik, R. A.; Hussain, M. A.; Rehman, Z. Revealing the Effects of microarc Oxidation on the Mechanical and Degradation Properties of Mg-Based Biodegradable Composites. *ACS Omega.* **2020**, *5* (23), 13694−13702.
(38) (38.) Shang, W.; Wu, F.; Wang, Y.; Rabiei Baboukani, A.; Wen, Y.; Jiang, J. Corrosion Resistance of Micro-Arc Oxidation/Graphene Oxide Composite Coatings on Magnesium Alloys. *ACS Omega.* **2020**, *5* (13), 7262−7270.
(39) Agarwal, R.; García, A. J. Biomaterial strategies for engineering implants for enhanced osseointegration and bone repair. *Adv. Drug Deliv Rev.* **2015**, *94*, 53−62.
(40) Zhang, J.; Ma, X.; Lin, D.; Shi, H.; Yuan, Y.; Tang, W.; Zhou, H.; Guo, H.; Qian, J.; Liu, C. Magnesium modification of a calcium phosphate cement alters bone marrow stromal cell behavior via an integrin-mediated mechanism. *Biomaterials.* **2015**, *53*, 251−264.
(41) Wang, J.; Xu, J.; Song, B.; Chow, D. H.; Shu-Hang Yung, P.; Qin, L. Magnesium (Mg) based interference screws developed for promoting tendon graft incorporation in bone tunnel in rabbits. *Acta Biomater.* **2017**, *63*, 393−410.
(42) Weber, F. E. Reconsidering Osteoconduction in the Era of Additive Manufacturing. *Tissue Eng. Part B Rev.* **2019**, *25* (5), 375−386.

https://doi.org/10.1021/acsomega.4c07635
ACS Omega 2024, 9, 46419−46428